

Developing 100 ps-resolved X-ray structural analysis capabilities on beamline NW14A at the Photon Factory Advanced Ring

Shunsuke Nozawa,^{a*} Shin-ichi Adachi,^{a,b} Jun-ichi Takahashi,^a Ryoko Tazaki,^a Laurent Guérin,^a Masahiro Daimon,^a Ayana Tomita,^c Tokushi Sato,^c Matthieu Chollet,^c Eric Collet,^d Hervé Cailleau,^d Shigeru Yamamoto,^b Kimichika Tsuchiya,^b Tatsuro Shioya,^b Hiroyuki Sasaki,^b Takeharu Mori,^b Kohei Ichianagi,^b Hiroshi Sawa,^b Hiroshi Kawata^b and Shin-ya Koshihara^{a,c}

Received 8 March 2007
Accepted 25 May 2007

^aNon-Equilibrium Dynamics Project, ERATO, Japan Science and Technology Agency, 1-1 O-ho, Tsukuba, Ibaraki 305-0801, Japan, ^bHigh Energy Accelerator Research Organization, 1-1 O-ho, Tsukuba, Ibaraki 305-0801, Japan, ^cTokyo Institute of Technology, 2-12-1 Oh-okayama, Meguro-ku, Tokyo 152-8551, Japan, and ^dGroupe Matière Condensée et Matériaux, UMR 6626 CNRS-Université Rennes 1, 35042 Rennes, France. E-mail: noz@post.kek.jp

NW14A is a newly constructed undulator beamline for 100 ps time-resolved X-ray experiments at the Photon Factory Advanced Ring. This beamline was designed to conduct a wide variety of time-resolved X-ray measurements, such as time-resolved diffraction, scattering and X-ray absorption fine structure. Its versatility is allowed by various instruments, including two undulators, three diffractometers, two pulse laser systems and an X-ray chopper. The potential for the detection of structural changes on the 100 ps time scale at NW14A is demonstrated by two examples of photo-induced structural changes in an organic crystal and photodissociation in solution.

© 2007 International Union of Crystallography
Printed in Singapore – all rights reserved

Keywords: photo-induced phase transition; time-resolved diffraction; time-resolved scattering; time-resolved XAFS; insertion device; PF-AR; TTF-CA; NiTTP.

1. Introduction

Time-resolved X-ray measurement is a powerful tool for the investigation of ultrafast science in various research fields ranging from local photochemical or photobiological processes, such as photodissociation (Schotte *et al.*, 2003; Chen *et al.*, 2001), to photo-induced phase transitions in crystals, including photo-induced insulator–metal transitions (Cavalleri *et al.*, 2004) and photo-induced ferroelectricity (Collet *et al.*, 2003). Time-resolved X-ray experiments that have been developed with the rapid progress of synchrotron sources have made it possible to study photo-induced ultrafast transformations by synchronizing X-ray pulses with ultrashort laser pulses (Bourgeois *et al.*, 1996; Wulff *et al.*, 1997; Siders *et al.*, 1999; Schoenlein *et al.*, 2000; Cavalleri *et al.*, 2005; Lindenberg *et al.*, 2005). This pump–probe synchronization can be combined with established X-ray techniques, such as diffraction, scattering and absorption experiments. Time-resolved X-ray diffraction, which enables direct access to the dynamics of electronic, atomic and molecular motions, provides a unique opportunity to obtain key information on the mechanism of transformations driven by a laser pulse (Srajer *et al.*, 1996; Techert *et al.*, 2001; Schotte *et al.*, 2003; Collet *et al.*, 2003). Time-resolved X-ray absorption fine structure (XAFS)

(Chen *et al.*, 2001; Saes *et al.*, 2003) and time-resolved scattering (Plech *et al.*, 2004; Ihee *et al.*, 2005) measurements are also important for studying the cluster dynamics as complementary experiments of time-resolved diffraction measurements.

The Photon Factory Advanced Ring (PF-AR) is a full-time single-bunch synchrotron radiation source operated for time-resolved X-ray studies with pulsed X-rays. By utilizing the full advantage of the sparse bunch structure of the PF-AR ring, the in-vacuum undulator beamline NW14A was constructed for time-resolved X-ray studies. The instrumentation developed at NW14A is described in this paper with two examples from time-resolved diffraction and XAFS experiments.

2. Design and performance of the NW14A beamline

2.1. Storage ring and overall design of the beamline

Time-resolved X-ray experiments using the bunch structure of the storage ring primarily require a relatively sparse bunch-filling. The 6.5 GeV PF-AR is fully operated in single-bunch mode for about 5000 h per year. Electrons with a ring current of 60 mA (75.5 nC per bunch) are stored in a single bucket with a lifetime of ~20 h. The radio frequency (RF) for cavities

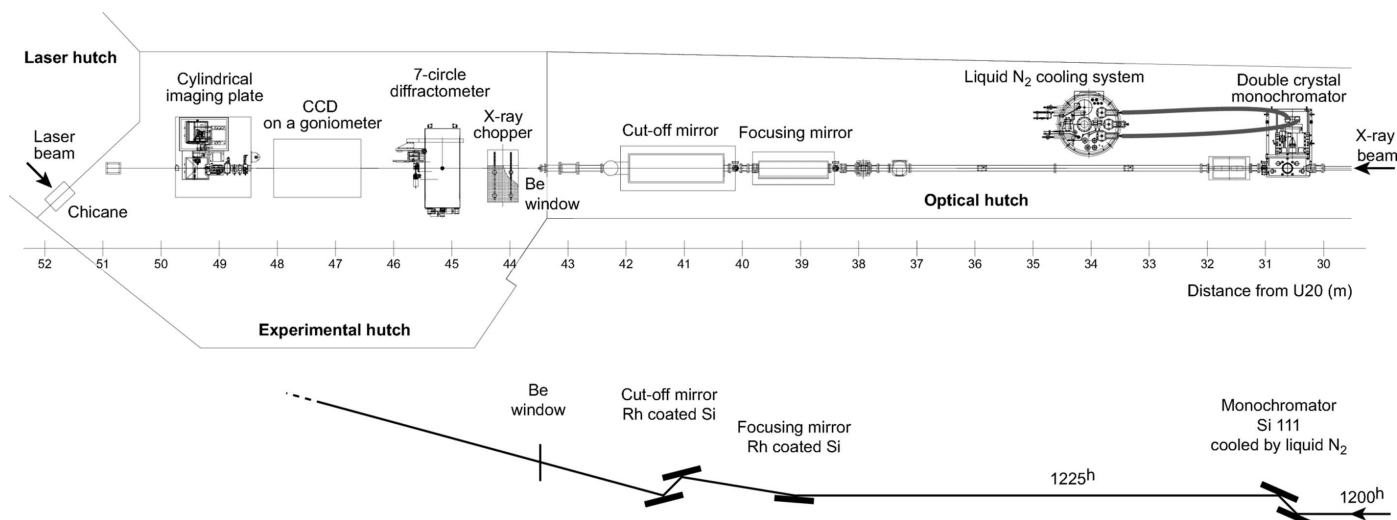


Figure 1 Schematic drawing of NW14A. The beam is monochromized by a double-crystal monochromator and then focused using a focusing mirror. Higher orders are rejected by a pair of flat mirrors.

Table 1 Source property and list of optical components.

Optical component	Position	Specifications
First undulator (U20)	0 m	In-vacuum undulator, energy range 13–18 keV with first harmonics
Second undulator (U36)	5.62 m	In-vacuum undulator, energy range 5–20 keV with first, third and fifth harmonics
Monochromator	30.62 m	Si(111) double-crystal monochromator with liquid-nitrogen cooling
Focusing mirror	39.12 m	Rhodium-coated silicon single crystal [toroidal, 1000 mm (L) × 100 mm (W) × 70 mm (T)] with 2.8 mrad glancing angle
Higher-order rejection mirror	41.12 m	Rhodium-coated silicon single crystal [flat, 1000 mm (L) × 100 mm (W) × 70 mm (T), a double-mirror system]

and harmonic number of the PF-AR are 508.58 MHz and 640, respectively. Therefore, the X-ray pulses are delivered at a frequency of 794 kHz with a pulse duration of about 100 ps [full width at half-maximum (FWHM)]. A schematic drawing of NW14A is shown in Fig. 1 and the specifications of the source and optical elements are listed in Table 1.

2.2. Insertion device and front-end

The beamline has two undulators with period lengths of 20 mm (U20) and 36 mm (U36). U20 gives the first harmonic in the energy range 13–18 keV. The energy bandwidth of the first harmonic is $\Delta E/E \approx 15\%$, which can be utilized as a ‘narrow-bandwidth white beam’ or a ‘wide-bandwidth monochromatic beam’. U36, which is used as a tunable and intense monochromatic X-ray source by use of a double-crystal monochromator and a focusing mirror, covers an energy range of 5–20 keV with the first, third and fifth harmonics. The measured photon flux from U36 and U20 at several gaps is shown in Fig. 2. The absolute photon flux was estimated by

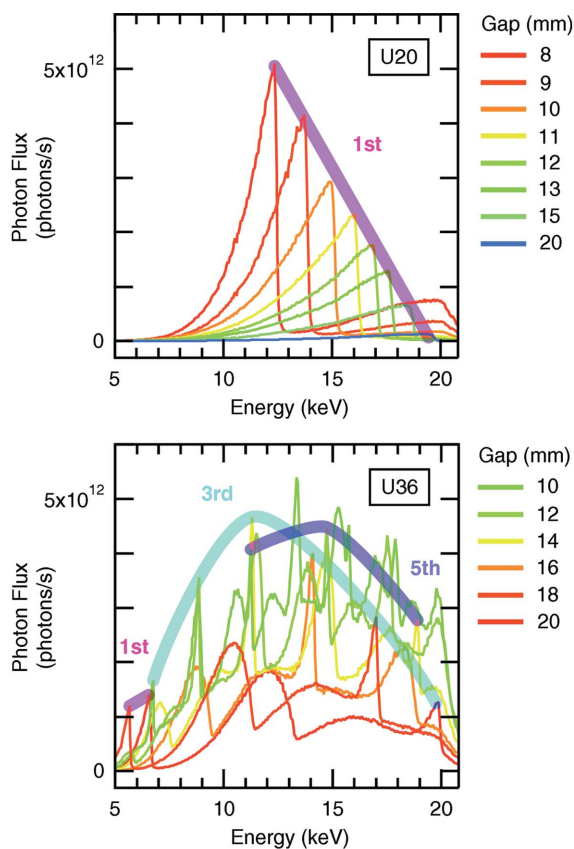


Figure 2 Measured photon flux from U20 and U36 at several gaps. The intensity was normalized by 60 mA of the ring current and 0.318 mrad (H) × 0.053 mrad (V) beam divergence. In U36 the photon flux at the gap of 18 mm was measured without one of the two graphite heat absorbers to increase the flux around 5 keV.

measuring the photocurrent using a PIN photodiode. The PIN photodiode was located at 43.7 m in the experimental hut, and the X-ray was focused on the surface of the PIN photodiode with a spot size of 500 μm (H) × 250 μm (V). The intensity was normalized to a 60 mA ring current and

0.318 mrad (H) \times 0.053 mrad (V) beam divergence. When the gap of U36 is wider than 18 mm, one of two graphite heat absorbers can be removed from the beam path because the heat load on the monochromator is relatively low. The spectrum from U20, which has a smooth energy distribution in the energy range 13–18 keV, is useful for experiments using a white beam, such as time-resolved Laue diffraction. In Fig. 2 the photon flux from U36 at 18 mm gap was measured without one of the graphite heat absorbers and, thus, the photon flux could be increased by one order of magnitude around 5 keV. In U36, more than 1×10^{12} photons s^{-1} of photon flux were produced in the energy range 5–20 keV by the first, third and fifth harmonics.

The front-end consists of a fixed mask, a beam-position monitor, two graphite heat absorbers, a beam shutter, XY slits for white X-rays, and double Be windows. The radiation power from the undulator can be reduced by the graphite heat absorber, the Be windows and by limiting the opening aperture.

The photon flux density estimated from the measured flux from U36 and U20 is shown in Fig. 3. The absorption of the graphite heat absorbers and Be windows, the reflectance of rhodium in the focusing mirror, and the bandwidths of the monochromator are taken into account in order to estimate the photon flux density. The intensity was normalized by

60 mA of the ring current and 1 mrad (H) \times 1 mrad (V) beam divergence.

2.3. X-ray optics

The main optical components are a double-crystal monochromator, a focusing mirror and a cut-off mirror, which are located 31.62 m, 44.62 m and 47.12 m from the center of insertion device U20, respectively. The monochromator consists of flat silicon (111) crystals, which are cooled by liquid nitrogen in order to reduce the deformation caused by heat load problems (Kawata *et al.*, 2004; Mochizuki *et al.*, 2001). The cooling system can handle heat loads up to 450 W.

A bent cylindrical mirror focuses the beam at the sample position. The mirror is coated with rhodium (100 nm thick). The mirror can be bent at a range of bending radii between -2000 m and $+2000$ m by a mechanical bender. A schematic view of the focusing mirror is shown in Fig. 4(a). The glancing angle is adjusted by tilting the mirror at the mirror's center. A bending mechanism directly applies the bending momentum to the mirror. The bending deflection is defined in Fig. 4(a). The beam size from U36 was measured with 0.318 mrad (H) \times 0.053 mrad (V) beam divergence. The focusing ratio was 4.53:1 as the focusing point and the center of the mirror were located 40.9 m and 33.5 m, respectively, away from U36. The horizontal beam size at several glancing angles θ is shown in Fig. 4(b). The glancing angle θ is represented as

$$\theta = \sin^{-1} \frac{R_s(L_1 + L_2)}{2L_1L_2}, \quad (1)$$

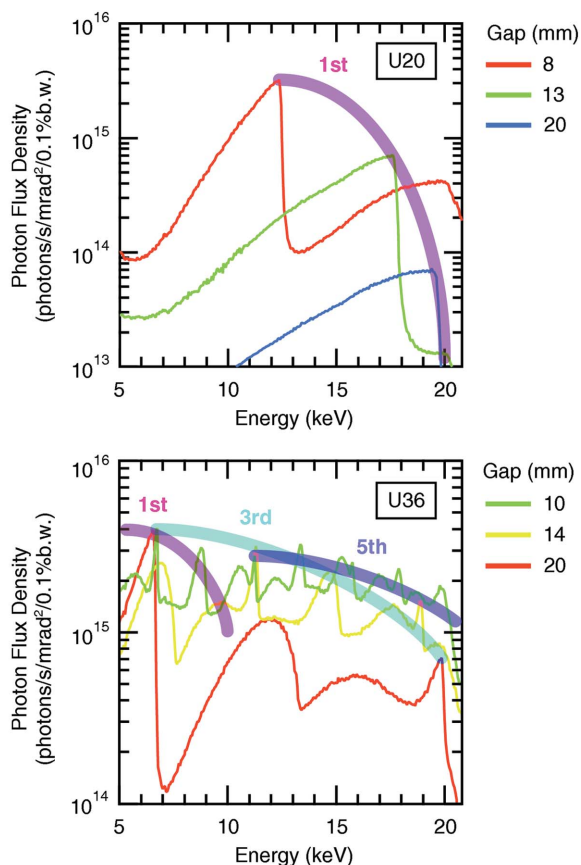


Figure 3 Photon flux density of the radiation from U36 and U20. The intensity was normalized by 60 mA of the ring current and 1 mrad (H) \times 1 mrad (V) beam divergence.

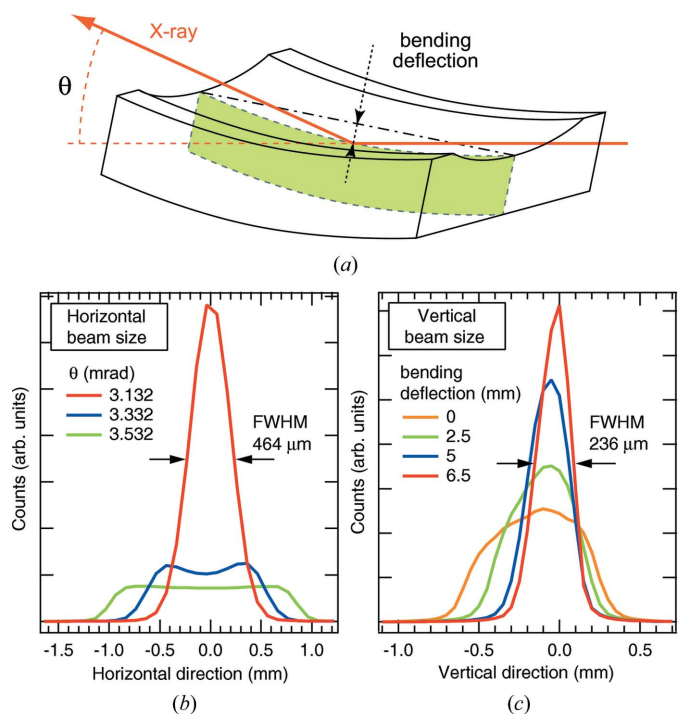


Figure 4 (a) Schematic view of the focusing mirror. (b) Horizontal beam size at several glancing angles θ . (c) Vertical beam size at several bending deflections. The glancing angle θ and the bending deflection are defined in (a).

where $R_s = 37.97$ mm is the sagittal radius of the cylindrical mirror, L_1 is the distance between U36 and the mirror, and L_2 is the distance between the mirror and the focusing point. The best horizontal focus was acquired with a glancing angle of 3.132 mrad as derived from the equation. The vertical beam size at several bending deflections is shown in Fig. 4(c), and the best vertical focus was acquired at 6.5 mm. The beam FWHMs are $464 \mu\text{m}$ (H) \times $236 \mu\text{m}$ (V), in agreement with the known mirror aberrations.

The cut-off mirror system consists of two flat mirrors to reduce contamination of the higher harmonics. Both mirror surfaces are coated with rhodium (100 nm thick). The inclination of each mirror is adjustable in the range 0–12 mrad. Consequently, it is possible to choose the cut-off energy from 4 to 20 keV without changing the direction of the monochromatic beam. The second mirror of the cut-off mirrors can also be bent by a mechanical bender in order to fix the vertical angle dispersion of the beam. InGa liquid metal is inserted between all of the X-ray mirrors and the water-cooled copper plate to obtain a good thermal contact. The number and thickness of the beryllium windows are reduced so as to minimize the low-energy limit; thus, X-rays between 5 and 20 keV can be used at NW14A.

2.4. Laser systems

NW14A has two pulse laser systems: a 150 fs Ti:sapphire regenerative amplifier laser system (Spectra Physics, Millennia-Tsunami-Spitfire-Evolution) and a Q-switched Nd:YAG laser (Continuum, Powerlite 8000). The Ti:sapphire laser system, which is operated at 800 nm fundamental wavelength, is capable of reaching up to 1 mJ pulse^{-1} with a repetition rate of 945 Hz. The laser is installed in a laser hutch next to the experimental hutch. An optical parametric amplifier (Light Conversion, TOPAS-C) for the 150 fs laser system is also installed in the laser hutch to enlarge the spectral range from visible to mid-infrared. The laser beam is brought to the sample in the experimental hutch through a chicane. The flash lamp of the YAG laser is externally triggered at 10 Hz, and 10 ns-wide 1 J laser pulses are obtained by cavity Q-switching. The YAG laser can be used near the sample in the experimental hutch because it is movable.

2.5. Synchronization of X-ray and laser pulses

The synchronization of X-ray and laser pulses is based on the RF master clock that drives the electron bunch in the storage ring. When the X-ray experiment is conducted with a 945 Hz Ti:sapphire laser and a detector with no gating such as a CCD or an imaging-plate detector, an X-ray chopper is required to synchronize the X-ray and the laser pulses at a 1:1 ratio. The timing block and the synchronization chart are shown in Fig. 5. The X-ray pulse is emitted every $1.26 \mu\text{s}$ ($794 \text{ kHz} = 508 \text{ MHz}/640$) from the PF-AR as shown in Fig. 5(i), because the harmonic number is 640. After the RF amplifier, the RF master clock is separated into two major timings: one for the laser system and the other for the X-ray chopper. In the X-ray chopper the 508 MHz RF signal and the

794 kHz revolution signal are used as the clock and bunch phase reference signal, respectively. A 945 Hz ($794 \text{ kHz}/840$) repetition frequency of the X-ray is then produced to match the frequency of the Ti:sapphire 150 fs laser system. The X-ray chopper, made by Forschungszentrum Jülich (Lindenau *et al.*, 2004), consists of a rotor furnished with a narrow channel for the beam passage. A novel feature of the chopper is its continuous phase locking with a timing jitter of less than 2 ns. The open time of the channel at the center of the tapered aperture is $1.64 \mu\text{s}$ with 945 Hz, as shown in Fig. 5(ii). If the frequency of the laser is slower than 945 Hz, such as that of the YAG laser system with a 10 Hz operation, synchronization between the X-ray and the laser pulses in a 1:1 ratio can be made by inserting a millisecond shutter (UNIBLITZ, XRS1S2P0) between the X-ray chopper and the sample. In the laser system, the mode-locked Ti:sapphire laser is operated as the seeding laser at 85 MHz ($508 \text{ MHz}/6$) and is guided to the

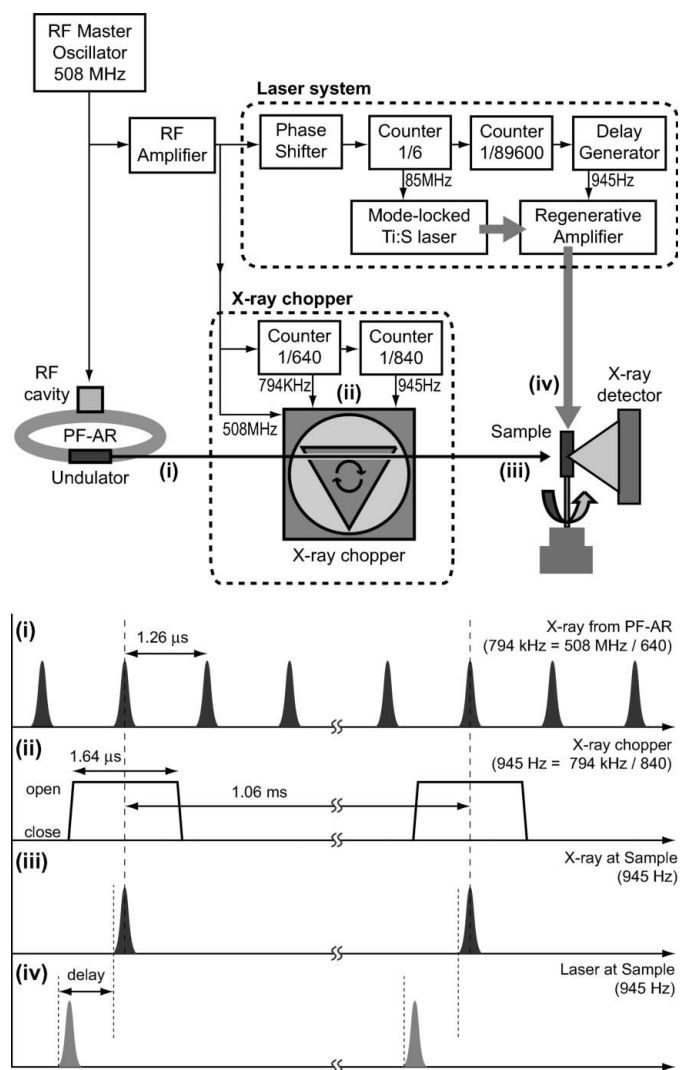


Figure 5 Timing block diagram (top) and chart (bottom) of the synchronization system when using the X-ray chopper to synchronize between 794 kHz X-rays and 945 Hz laser pulses in a 1:1 ratio. Timing chart of the X-rays from PF-AR (i), the X-ray chopper (ii), the X-rays at the sample (iii), and the laser at the sample (iv).

regenerative amplifier. The laser pulse, which is synchronized with the pulse X-ray, is generated to pump the regenerative amplifier by the Q-switched Nd:YLF laser triggered at 945 Hz (85 MHz/89600). Then, 945 Hz laser pulses are brought into the sample position by some mirrors with a light path of about 10 m. Double-pulse trains, which consist of laser pulses and probing X-ray pulses at the sample, are shown in Figs. 5(iii) and 5(iv). Any delay between the double-pulse trains is controlled by changing the emission timing of the pulse laser with a delay generator, counter (1/6) and an analog phase shifter. The fine control of the relative delay on the 100 ps time scale is achieved using a phase shifter, which controls the RF phase electrically.

2.6. Monitoring timing

The timing of the X-ray and the laser was measured using a InGaAs metal–semiconductor–metal (MSM) photodetector (Hamamatsu, G7096) coupled to a high-frequency preamplifier and a 2.5 GHz digital oscilloscope (Tektronix, DPO7254). The typical rise time of the photodetector is 40 ps, which is faster than the X-ray duration. The diode was set at the sample position. The guard glass in front of the diode was removed to increase the sensitivity of the X-ray below 10 keV. A signal waveform recorded by the diode with 50 Ω load impedance is shown in Fig. 6, where the laser and the X-ray pulses are separated by 6.4 ± 0.1 ns. The 0.1 ns time resolution of NW14A is attributed to the pulse width of the X-ray because the total jitter is less than 0.1 ns. The diode is also used to check the phase difference between the arrival X-ray and the channel of the X-ray chopper at the position of the chopper. When the X-ray is out of phase with the chopper, the phase is adjusted by monitoring the signal waveform from the oscilloscope and varying the delay of the chopper.

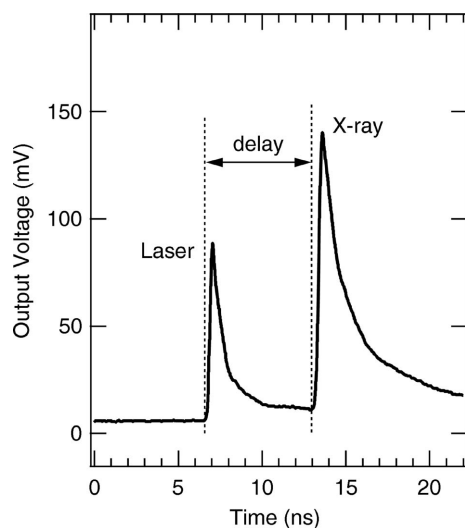


Figure 6 Monitoring the signal recorded by the InGaAs MSM photodetector. The laser pulse is separated from the X-ray pulse by 6.4 ± 0.1 ns. The exact delay between the laser and the X-ray pulse is measured between the leading edge of the laser and the X-ray pulse.

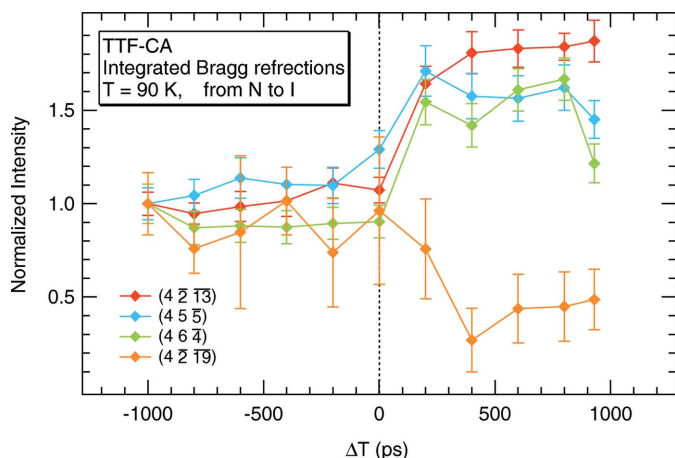
2.7. Diffractometers

NW14A has three diffractometers: a MarCCD 165 with a MarDTB (Mar USA), an imaging-plate (IP) diffractometer (Rigaku, RAPID-SR3) and a seven-circle diffractometer (HUBER). Time-resolved measurements can be conducted with all diffractometers combined with the pulsed laser system. The data set for the structural analysis can be measured by the CCD with a 16-bit analog-to-digital converter (ADC). The readout time of the CCD is about 2.5 s. The CCD image has 2048×2048 pixels with a $80 \mu\text{m} \times 80 \mu\text{m}$ pixel size. The camera length can be adjusted from 20 mm to 370 mm, and the maximum 2θ angle is 106° . When a diffraction image with a wide dynamic range is required for the charge density analysis, the IP diffractometer with a 20-bit ADC is suitable for the experiment. It has a $683 \text{ mm} \times 350 \text{ mm}$ cylindrical shape with a $100 \mu\text{m} \times 100 \mu\text{m}$ pixel size. The camera length is fixed at 191 mm, and the maximum 2θ angle is 145° . The goniometer of the IP diffractometer is a three-circle (φ , ω and χ) goniometer. Although the readout time is about 5 min, a high-accuracy diffraction image can be acquired in a single scan. The seven-circle diffractometer has a conventional four-circle (φ , ω , χ and 2θ) diffractometer with an additional three-circle diffractometer on the 2θ arm for polarization analysis. This diffractometer system has a long 2θ arm with an angle resolution of 0.0001° and is utilized for mapping scans in reciprocal space, diffuse scattering observations or high-resolution powder patterns with a point detector, such as a scintillation counter or an avalanche photodiode. The sample can be cooled to 30 K by using a cryogenic helium gas flow (Japan Thermal Engineering, XR-HR10K) or closed-cycle He cryostat with a half-spherical Be dome shroud on the seven-circle diffractometer.

3. Feasibility of pump–probe X-ray experiments

3.1. Photo-induced structural changes in TTF-CA

In order to demonstrate the feasibility of time-resolved X-ray crystallography at NW14A, a time-resolved structural analysis of a tetrathiafulvalene-chloranil (TTF-CA) crystal has been conducted using the X-ray chopper, the CCD and the 150 fs laser system. A neutral (N)–ionic (I) phase transition of around 80 K is observed in TTF-CA owing to the competition between the energy gain of the long-range Coulomb attractive interaction and the effective ionization energy of the donor–acceptor pair (Koshihara *et al.*, 1990). This transition can be reversibly triggered by the pulse laser excitation (Koshihara *et al.*, 1990; Iwai *et al.*, 2002; Collet *et al.*, 2003; Guérin *et al.*, 2004). A time-resolved measurement of the Bragg intensities in the neutral phase of TTF-CA was carried out at 90 K. The set-up and the timing chart of this experiment are the same as those in Fig. 5. A $100 \mu\text{m} \times 60 \mu\text{m} \times 40 \mu\text{m}$ single crystal was pumped using the Ti:sapphire laser at 800 nm with the light polarization parallel to the stacking axis of TTF-CA. Laser pulses of 1.5×10^{16} photons cm^{-2} pulse $^{-1}$ were delivered to the sample. The monochromatic X-ray (18 keV) flux on the sample was 3×10^9 photons s^{-1} when using the X-ray

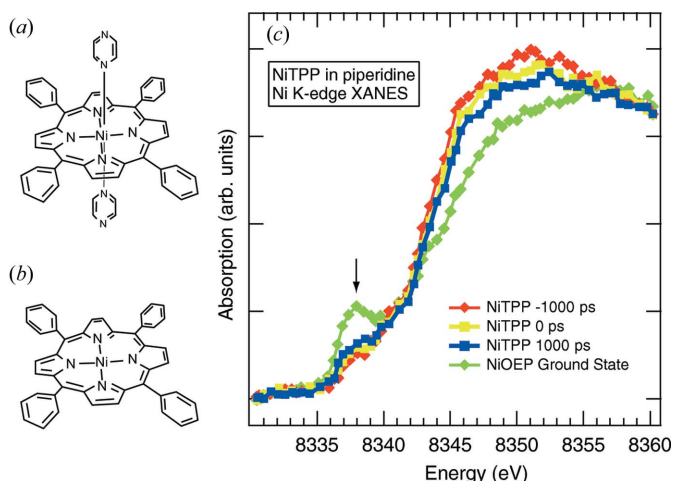

Figure 7

Time profiles of the integrated diffraction intensity. The change in intensity is attributed to the photo-induced three-dimensional structural reorganization from the N phase to the I phase.

chopper. The X-ray diffraction patterns were collected using a CCD camera. For each delay, five frames were collected with 5 s of exposure and a 2° oscillation step. The time profiles of the integrated diffraction intensity are shown in Fig. 7, where a dramatic change in the intensities after the laser excitation is observed. This behavior is a direct signature of a strong three-dimensional structural reorganization in the photo-induced state, and it shows the good reproducibility of the previous results (Collet *et al.*, 2003; Guérin *et al.*, 2004).

3.2. Photodissociation in NiTPP

If a detector with gating capabilities, such as an avalanche photodiode or a fast scintillation counter, is used, the X-ray chopper is not necessary and a gated integrator system can be used instead (Saes *et al.*, 2003). In order to demonstrate the feasibility of a time-resolved X-ray experiment without an X-ray chopper, a time-resolved molecular structural analysis of NiTPP(Pip)₂ (NiTPP, nickel tetraphenylporphyrin; Pip, piperidine) was conducted by means of time-resolved XAFS measurements. In the ground state the divalent Ni ion adopts a triplet spin state T^0 [NiTPP(Pip)₂ shown in Fig. 8(a)]. The excited state is induced by the laser pulse and then, through some transient states, a singlet spin state S^0 [NiTPP shown in Fig. 8(b)] is produced by ejecting both axial ligands. This process proceeds within a few hundred picoseconds (Rodríguez & Holten, 1990). The S^0 state is unstable in strong coordinating solvents, and the system will return to T^0 within 28 ns. The time-resolved Ni *K*-edge X-ray absorption near-edge structure (XANES) spectra were measured by using a scintillation counter, a gated integrator and a 150 fs laser system. Through the metal filter and the solar slit, the fluorescence signal was detected by the fast scintillation counter, which has a 50 mm diameter of acceptance surface. The fluorescence signal just after (or just before) the laser pulse was chosen by the gated integrator synchronized with the laser pulse (945 Hz). The XANES spectrum was obtained by counting the output voltage from the gated integrator through a voltage-to-frequency converter. The 1 mM solution of


Figure 8

(a) Geometry of the NiTPP(Pip)₂ molecule. (b) Geometry of the NiTPP molecule. (c) XANES spectra of NiTPP in piperidine and NiOEP in pyridine. The ground states of NiTPP in piperidine and NiOEP in pyridine show sixfold and fourfold coordination, respectively. In the NiTPP spectra the intensity of the pre-edge peak indicated by the arrow increases and the main-edge structure from 8345 to 8355 eV changes after the excitation. This is a direct signature of the photodissociation in NiTPP from the T^0 to S^0 state.

NiTPP(Pip)₂ was pumped with the second-harmonic generation of a Ti:sapphire laser at 400 nm. Laser pulses of 5×10^{15} photons cm^{-2} pulse^{-1} were delivered to the sample. The monochromatic X-ray (around 8.3 keV) flux on the sample was 2×10^{12} photons s^{-1} at 794 kHz. The countable signal was reduced 840 times from its original fluorescence signal when using the gated integrator. The Ni *K*-edge XANES spectra of NiTPP at several delays and the ground state of NiOEP (nickel octaethylporphyrin) in the pyridine are shown in Fig. 8(c). The ground states of NiTPP in piperidine and NiOEP in pyridine show sixfold and fourfold coordination, respectively. The pre-edge peak indicated by the arrow represents the localized $4p_z$ orbital. The intensity of the pre-edge peak in NiTPP increases after the excitation because the axial ligand, which hybridizes with the $4p_z$ orbital, is dissociated. The main-edge structure from 8345 to 8355 eV consists of the σ^* molecular orbital, and its structure also changes after excitation because the σ_z orbital disappears by the dissociation of the axial ligand. Both photo-excited changes appeared in the pre-edge and main edge towards the spectrum of NiOEP, and this is a direct signature of the photodissociation from the T^0 to S^0 state with a good reproducibility (Chen *et al.*, 2001). One of the important points to emphasize in this measurement is that an XANES spectrum could be measured in 10 min by the above-mentioned system with the fast scintillation counter and the gated integrator, although it normally takes a few hours to obtain an XANES spectrum with the equivalent signal-to-noise ratio using a photon-counting method.

4. Conclusions

At PF-AR, the capability for the investigation of structural dynamics on the 100 ps time scale has been demonstrated.

Capabilities for dynamical studies such as those presented in this paper can be utilized for all user experiments (~5000 h per year) at PF-AR. Unlike any other beamlines in the world, the amount of user beam time for time-resolved X-ray experiments at PF-AR is incredibly high. Instrumentation for such studies has been successfully developed, and a time-series of diffraction data sets has been collected to produce a 'movie' of photoreactions at atomic resolution. Further analysis of the structural dynamics is currently in progress.

This research was supported by grants from the Japanese Ministry of Education, Culture, Sports, Science and Technology (SA) and performed under the approval of the Photon Factory Program Advisory Committee (PF-PAC No. 2004S1-001).

References

- Bourgeois, D., Ursby, T., Wulff, M., Pradervand, C., Legrand, A., Schildkamp, W., Labouré, S., Srajer, V., Teng, T. Y., Roth, M. & Moffat, K. (1996). *J. Synchrotron Rad.* **3**, 65–74.
- Cavaliere, A. L. *et al.* (2005). *Phys. Rev. Lett.* **94**, 114801.
- Cavalleri, A., Chong, H. H. W., Fourmaux, S., Glover, T. E., Heimann, P. A., Kieffer, J. C., Mun, B. S., Padmore, H. A. & Schoenlein, R. W. (2004). *Phys. Rev. B*, **69**, 153106.
- Chen, L. X., Jäger, W. J. H., Jennings, G., Gosztola, D. J., Munkholm, A. & Hessler, J. P. (2001). *Science*, **292**, 262–264.
- Collet, E., Lemée-Cailleau, M.-H., Buron-Le Cointe, M., Cailleau, H., Wulff, M., Luty, T., Koshihara, S., Meyer, M., Toupet, L., Rabiller, P. & Techert, S. (2003). *Science*, **300**, 612–615.
- Guérin, L., Collet, E., Lemée-Cailleau, M.-H., Buron-Le Cointe, M., Cailleau, H., Plech, A., Wulff, M., Koshihara, S. & Luty, T. (2004). *Chem. Phys.* **299**, 163–170.
- Ihee, H., Lorenc, M., Kim, T. K., Kong, Q. Y., Cammarata, M., Lee, J. H., Bratos, S. & Wulff, M. (2005). *Science*, **309**, 1223–1227.
- Iwai, S., Tanaka, S., Fujinuma, K., Kishida, H., Okamoto, H. & Tokura, Y. (2002). *Phys. Rev. Lett.* **88**, 057402.
- Kawata, H., Mori, T., Adachi, H., Matsugaki, N., Koyama, A. & Nomura, M. (2004). *AIP Conf. Proc.* **705**, 663–666.
- Koshihara, S., Tokura, Y., Mitani, T., Saito, G. & Koda, T. (1990). *Phys. Rev. B*, **42**, 6853–6856.
- Lindenau, B., Rübiger, J., Polachowski, S. & Fremerey, J. K. (2004). *AIP Conf. Proc.* **705**, 1019–1022.
- Lindenberg, A. M. *et al.* (2005). *Science*, **308**, 392–395.
- Mochizuki, T., Kohmura, Y., Awaji, A., Suzuki, Y., Baron, A., Tamasaku, K., Yabashi, M., Yamazaki, H. & Ishikawa, T. (2001). *Nucl. Instrum. Methods, A* **467–468**, 647–649.
- Plech, A., Wulff, M., Bratos, S., Mirloup, F., Vuilleumier, R., Schotte, F. & Anfinrud, P. A. (2004). *Phys. Rev. Lett.* **92**, 125505.
- Rodriguez, J. & Holten, D. (1990). *J. Chem. Phys.* **92**, 5944–5950.
- Saes, M., Bressler, C., Abela, R., Grolimund, D., Johnson, S. L., Heimann, P. A. & Chergui, M. (2003). *Phys. Rev. Lett.* **90**, 047403.
- Schoenlein, R. W., Chattopadhyay, S., Chong, H. H. W., Glover, T. E., Heimann, P. A., Shank, C. V., Zholents, A. A. & Zolotarev, M. S. (2000). *Science*, **287**, 2237–2240.
- Schotte, F., Lim, M., Jackson, T. A., Smirnov, A. V., Soman, J., Olson, J. S., Phillips, G. N. Jr, Wulff, M. & Anfinrud, P. A. (2003). *Science*, **300**, 1944–1947.
- Siders, C. W., Cavalleri, A., Sokolowski-Tinten, K., Tóth, Cs., Guo, T., Kammler, M., Horn von Hoegen, M., Wilson, K. R., von der Linde, D. & Barty, C. P. J. (1999). *Science*, **286**, 1340–1342.
- Srajer, V., Teng, T.-Y., Ursby, T., Pradervand, C., Ren, Z., Adachi, S., Schildkamp, W., Bourgeois, D., Wulff, M. & Moffat, K. (1996). *Science*, **274**, 1726–1729.
- Techert, S., Schotte, F. & Wulff, M. (2001). *Phys. Rev. Lett.* **86**, 2030–2033.
- Wulff, M., Schotte, F., Naylor, G., Bourgeois, D., Moffat, K. & Mourou, G. (1997). *Nucl. Instrum. Methods, A* **398**, 69–84.